Title

Diffusion Barriers for Carbon Monoxide on the Cu(001) Surface Using Many-Body Perturbation Theory and Various Density Functionals

Journal

Journal of Chemical Theory and Computation, 17(12)

ISSN

1549-9618

Authors

Wei, Ziyang
Göltl, Florian
Sautet, Philippe

Publication Date

2021-12-14

DOI

10.1021/acs.jctc.1c00946

Diffusion Barriers for Carbon Monoxide on the Cu(001) Surface Using Many Body Perturbation Theory and Various Density Functionals

Ziyang Wei,[†] Florian Göltl,[*,‡] and Philippe Sautet[*,†,¶]

†*Department of Chemistry and Biochemistry, University of California, Los Angeles, California, 90095, United States*

‡*Department of Biosystems Engineering, The University of Arizona, Tucson, Arizona, 85721, United States*

¶*Department of Chemical and Biomolecular Engineering, University of California, Los Angeles, California, 90095, United States*

E-mail: fgoeltl@arizona.edu; sautet@ucla.edu

Abstract

First principles calculations play a key role in understanding the interactions of molecules with transition metal surfaces and the energy profiles for catalytic reactions. However, many of the commonly used density functionals are not able to correctly predict the surface energy as well as the adsorption site preference for a key molecule such as CO, and it is not clear to what extent this shortcoming influences the prediction of reaction or diffusion pathways. Here, we report calculations of carbon monoxide diffusion on the Cu(001) surface along the [100] and [110] pathways, as well as the surface energy of Cu(001), and CO adsorption energy and compare the performance of the PBE, PBE+D2, PBE+D3, RPBE, BEEF-vdW, HSE06 density functionals and the

Random Phase Approximation (RPA), a post Hartree-Fock method based on many-body perturbation theory. We critically evaluate the performance of these methods and find that RPA appears to be the only method giving correct site preference, overall barrier, adsorption enthalpy and surface energy. For all the other methods, at least one of these properties is not correctly captured. These results imply that many DFT based methods lead to qualitative and quantitative errors in describing CO interaction with transition metal surfaces, which significantly impacts the description of diffusion pathways. It is well conceivable that similar effects exist when surface reactions of CO related species are considered. We expect that the methodology presented here will be used to get more detailed insights into reaction pathways for CO conversion on transition metal surfaces in general and Cu in particular, which will allow us to better understand the catalytic and electrocatalytic reactions involving CO related species.

Introduction

Transition metal catalysts are among the prime candidates in the conversion of CO to various hydrocarbons, either through thermal catalysis in the conversion of synthesis gas[1–4] and the water-gas shift reaction,[5,6] or electrocatalysis in the CO and CO_2 reduction reaction.[7] In these processes, multiple reactions take place simultaneously on the surface and only a detailed understanding of this reaction network allows to identify predominant reaction pathways, reaction rate, and product selectivity. In this context, first principles modeling[8,9] plays a key role, since it is a method that can assign reaction energies and barriers to all possible reaction steps. When combining this information with microkinetic modeling[10,11] or kinetic Monte Carlo simulations,[12] it is then possible to predict reaction rates and selectivities for a specific catalytic system.

Density Functional Theory (DFT)[13,14] in its Generalized Gradient Approximation[15] has become the most commonly used method to model surface reactions, due to a reasonable accuracy paired with a high computational efficiency. However, it is reported that many

DFT-based methods fail in capturing the correct adsorption site preference of CO on several metal surfaces,[16–19] which is often referred to as the CO-adsorption puzzle. While the incorrect prediction of the relative stability of CO adsorption to different high-symmetry surface sites is already concerning in its own right, it also poses the question, to what degree other aspects of CO interactions with metal surfaces, such as surface reactions or molecular diffusion, are influenced by this shortcoming.

A good example for these problems is the interactions of CO with Cu surfaces. CO interactions with Cu surfaces are of particular interest, since Cu is the main component of the industrial catalyst for methanol synthesis from synthesis gas[1–4] and the water-gas shift reaction,[5,6] and plays a key role for the electroreduction of CO_2 into C_1[20–22] or C_2[23,24] products. A main controversy for Cu is the diffusion of CO on the Cu(001) surface. At an experimental level, Graham and Toennies[25] report a minimum diffusion pathway from the top over the bridge site, while Alexandrowicz et al.[26] identify the diffusion over the fourfold coordinated hollow site as energetically more favorable. Subsequently, this dispute has drawn significant interest from the theory community, who have arrived at different conclusions considering the shape of the potential energy surface for CO diffusion, a debate that has not been settled so far. However, the computational efforts were made based on GGA DFT energetics[27–29] and suffer from the wrong prediction of CO adsorption site preference.

One way to resolve this dispute is to move to post-Hartree-Fock methods.[30] In particular the Random Phase approximation (RPA),[31,32] a post-HF method that is based on many-body perturbation theory,[33,34] is a promising approach to address surface catalysis problems, since an implementation for plane waves in periodic boundary conditions exists.[35,36] On top of that, RPA is the only method that correctly predicts the surface energy of Cu(111) and adsorption of CO in the top position on Cu(111) and multiple other late transition metal surfaces.[37]

In this contribution, we use RPA to study the Cu(001) surface energy as well as the adsorption and diffusion of CO on the Cu(001) surface. In a first step, we discuss the

challenges for RPA calculations on transition metal surfaces and propose a k-space embedding scheme to reduce computational cost. Subsequently, we apply this methodology to the diffusion of CO along the [110] and [100] directions of the Cu(001) surface. We compare the RPA results with different DFT exchange correlation functionals including the Perdew-Burke-Ernzerhof (PBE) functional,[38] the PBE functional with D2[39] or D3[40] correction, the RPBE functional,[41] the Bayesian error estimation functionals (BEEF-vdW),[42] the strongly constrained and appropriately normed (SCAN) functional,[43] and Heyd-Scuseria-Ernzerhof (HSE06) functional.[44] All these results are then compared with experimental measurements in the literature.

Methods

Theory

In this contribution, we calculate total energies using the Adiabatic Connection Fluctuation Dissipation Theorem (ACFDT)[33,34] in its RPA, a method originating from many-body perturbation theory that has been reformulated within the framework of density functional theory. The total energy expression within RPA can be written as[35,36]

$$E^{RPA} = E^{EXX}([\phi_{occ}]) + E_c^{RPA}([\phi_{occ}, \phi_{uocc}]) \tag{1}$$

where E^{RPA} denotes the RPA total energy. This energy is composed of E^{EXX} the exact exchange energy, which only depends on the occupied orbitals ϕ_{occ}, and the RPA correlation energy E_c^{RPA}, which depends on all occupied and unoccupied orbitals ϕ_{occ}, ϕ_{uocc}.[45,46]

The focus on occupied and unoccupied orbitals leads to two challenges: First, the true orbitals are unknown, and they are typically approximated by orbitals obtained from semi-local DFT functionals.[35,47–50] Second, in principle an infinite number of unoccupied orbitals exists, and all orbitals need to be considered to arrive at an accurate E_c^{RPA}. However, evalu-

ating expressions for an infinite number of orbitals is not possible in a realistic computational setting. In practical implementations, E_c^{RPA} is evaluated at different orbital cut off energies E_{cut}^{χ}, and is extrapolated to an infinite orbital cut-off energy using

$$E_c^{RPA}(E_{cut}^{\chi}) = E_c^{RPA}(\infty) + \frac{A}{{E_{cut}^{\chi}}^{\frac{3}{2}}} \tag{2}$$

Even though E_c^{RPA} is extrapolated to infinite orbital cut-off energy, extrapolations based on higher E_{cut}^{χ} values improve the accuracy. At the same time, a higher E_{cut}^{χ} significantly increases the cost of calculations and in many cases makes the modeling of extended, periodic systems unfeasible. One option to circumvent this problem is to only model a small part of a periodic system at a high level and embed the small part in the fully periodic system modeled at a lower level of theory. At the most basic level, this approach has been introduced as the ONIOM approach,[51,52] where the energy of the total system is corrected by the energy difference between high-level and low level methods for the cluster description.[53–55] However, the geometry of a small cluster does not correctly capture the symmetry of an extended metallic system leading to delocalized wavefunctions. To address these issues, a density embedding scheme was developed by Carter et al.[56–61] to address these shortcomings and to more accurately treat metal surfaces. However, this approach still did not address the fundamental symmetry mismatch between the embedded cluster and the metallic surface and required significant effort to account for the delocalized wavefunctions. Hence, an approach that naturally matches the symmetry of the model system would be highly desirable.

In this contribution we choose such an approach: extended metals are best modeled using periodic boundary conditions. Here, a unit cell is used, which directly interacts with its adjacent mirror images. If only one unit cell was present, the delocalized nature of the wave functions, which often extend far further than the dimensions of a single unit cell, could not be correctly captured. This shortcoming is compensated by working in reciprocal space and treating multiple k-points. From a real space perspective, the number of k-points

indicates, how many multiples of the unit cell are considered in each direction when solving quantum mechanical equations. At the same time, the number of k-points included in the computational modeling is directly correlated to the computational cost and in particular for high cut-off RPA calculations, using a dense k-point mesh is often not feasible.

To address this problem, we apply an ONIOM like embedding scheme in k-space,[62] as shown in Scheme 1, named after the ONIOM scheme developed for real space embedding.[51,52] In this approach we start modeling our system using RPA with a maximum E_{cut}^{χ} value of 150 eV and a 3×3×1 k-point mesh. Subsequently, we embed these calculations in RPA calculations with a maximum E_{cut}^{χ} value of 100 eV and an 8×8×1 k-point mesh, and finally, we embed these two calculations in PBE model using a 15×15×1 k-point mesh. Using this approach, we express the RPA energy as

$$\begin{aligned} E^{RPA}(150\ eV, 15\times15\times1) = E^{RPA}(150\ eV, 3\times3\times1)+ \\ E^{RPA}(100\ eV, 8\times8\times1) - E^{RPA}(100\ eV, 3\times3\times1)+ \\ E^{PBE}(15\times15\times1) - E^{PBE}(8\times8\times1) \end{aligned} \tag{3}$$

In this expression, the first number in brackets refers to the maximum E_{cut}^{χ} value, while the second set of numbers refers to the k-point mesh used. Since we are studying a metallic slab extended in x and y direction, only one k-point is used in z direction.

Throughout this manuscript, we will also report values calculated using the different functionals along with the energetics of each embedding step for all calculations. This approach allows us to better understand the impact of using RPA and of potential compromises in computational setup on the observed diffusion energetics. The convergence test of energetics with respect to E_{cut}^{χ} can be found in the SI, table S1, and numerical validation of k-space ONIOM like like approach is provided in the SI, Table S2. Errors from applying the k-space ONIOM like scheme are estimated to be below 15 meV.

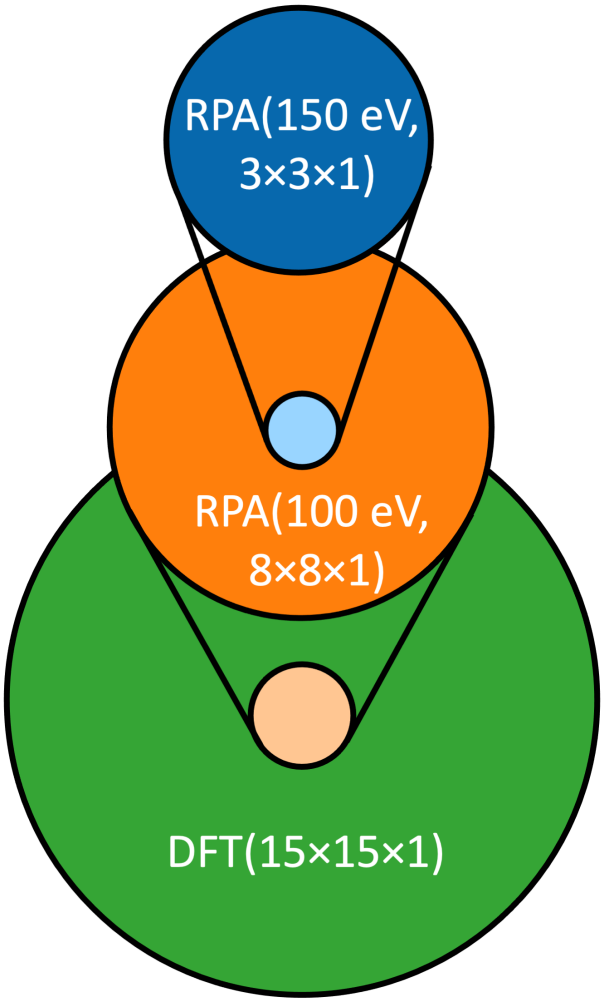

Scheme 1: Schematic representation of the extrapolations applied for the RPA calculations using different k-point meshes in this work. The applied approach shows large similarities to the ONIOM scheme, with the embedding being performed in k-space. The text indicates the used level of theory, and numbers in brackets indicate k-point meshes for RPA and PBE calculations, and cutoff energy values for RPA calculations.

Computational Models

As mentioned above, we calculate three different properties and compare them to experimental measurements, namely the surface energy of Cu(001), the adsorption strength of CO to Cu(001), and the diffusion barriers along the [100] and [110] directions of the Cu(001) surface. In this section, we describe the models chosen to calculate these different properties.

Surface Energy

The surface energy is calculated as

$$E_\sigma = \frac{E_{slab} - n * E_{bulk}}{\sigma} \tag{4}$$

where E_{slab} is the energy of a symmetric slab with two equivalent surfaces, and n is the number of atoms in this slab. E_{bulk} is the bulk energy per atom and σ is the surface area.

Bulk energies were calculated using a face centered cubic primitive unit cell containing one Cu atom with a 14×14×14 k-point mesh. Careful tests reveal that further increasing the k-point density only leads to small changes in energy (<1 meV). For this unit cell, lattice parameters were determined for most functionals. Only for HSE06 and RPA calculations, equilibrium lattice parameters reported in the literatures were used, namely 3.626 Å for HSE06[63] and 3.581Å for RPA.[36] For calculations with other functionals, the equilibrium lattice parameters were determined using a seven-point fit to a Birch-Murnaghan equation of state, where the lattice parameter in the calculations was varied by ±15%. Lattice parameters for all methods are reported in the Supporting Information, Table S3. Our PBE lattice parameter, 3.629 Å matches well with previous literatures, 3.630 Å.[36,63]

Energies of the slab were calculated for a six layer slab exposing a 1×1 Cu(001) surface. In this slab the two center layers were kept fixed and the outer two layers of the slab were allowed to relax. For most functionals, we first performed the structural optimizations with a 20×20×1 k-point mesh and reported total energies for calculations with a 30×30×1 k-point mesh. HSE06 and RPA energies were single point energies based on PBE optimized structures (using HSE06 and RPA lattice parameters) with a 20×20×1 k-point mesh. For most functionals, we increased the cutoff energy of the plane wave basis to 700 eV. Only for RPA and HSE06 calculations a cutoff energy as 550 eV was used.

CO adsorption

We calculate interactions between CO and the Cu(001) in a 2×2 unit cell (see Fig. 1 (a)) of a four layer slab. We use the experimental lattice constant of 3.615 Å[63] for all the functionals. This value is a good compromise between the PBE value, 3.629 Åand the RPA value, 3.581 Å.[37] This choice ensures that the RPA and PBE energetics in the embedding scheme are corresponding to comparable structures. Repeated images of the slabs are separated by 13 Å (21 Å) for RPA (and DFT). In DFT calculations, dipole corrections were applied. For RPA, dipole corrections are not available. In the past, Lébegue et al.[64] have shown that the correlation energy uncertainty is ca. 0.2 meV for vacuum separations larger than 13 Å. We performed test for slabs separated by 12/13/14 Å of vacuum using RPA and find convergence of results within 4 meV. Numerical values for convergence tests are provided in the SI Table S4. In the optimization process, the bottom two layers of Cu atoms are kept fixed and the top two layers are relaxed. In all calculations one CO molecule was placed in each unit cell, which leads to a coverage of 0.25. For the CO adsorption and diffusion calculations, a cutoff energy for the plane wave basis of 700 eV was used for SCAN calculations as it improves the quality of diffusion profile whereas a cutoff energy of 550 eV was used for other DFT calculations: PBE, PBE+D2, PBE+D3, RPBE, BEEF-vdW, and HSE06.

The adsorption enthalpy is calculated as

$$H_{ads} = E_{slab+CO} - E_{slab} - E_{CO} + \Delta ZPE + E_{correction}, \tag{5}$$

where the ΔZPE is the difference of zero-point energy of CO in gas phase and on the surface, which was calculated within the harmonic approximation. We calculated ΔZPE at PBE level of theory and tests using RPBE show changes in ΔZPE of less than than 1 meV. $E_{correction}$ summarizes an extrapolation from 4 layer to 6 layer results and (for RPA and HSE06) corrections for a denser k-point mesh. Numerical values for all components of H_{ads} are reported in the Supporting Information Table S5. All adsorption enthalpies are

reported for CO adsorption in the top position. Structures of the slab and CO adsorbed on the slab for methods other than HSE06 and RPA were firstly optimized using a 10×10×1 k-point mesh. Final energies were reported for an increased k-point mesh of 15×15×1. We assumed structural convergence for forces lower than 0.01 eV/Å. HSE06 and RPA energies were single point energies based on PBE optimized structures using an 8×8×1 k-point mesh.

For all DFT methods, the energy of a CO molecule reference energy was calculated using a 11×12×13 Å^3 supercell to suppress the spurious interactions between periodic images. RPA calculations relied on optimized PBE structures, and the values were extrapolated to the isolated molecule limit based on a series of calculations with different box sizes (7×8×9 Å^3, 8×9×10 Å^3, 9×10×11 Å^3, and 10×11×12 Å^3 for E_{cut}^{χ} =200 eV and 250 eV, and additional 11×12×13 Å^3 for E_{cut}^{χ} =100 eV and 150 eV). Molecular calculations were performed with a $\mathbf{\Gamma}$ point only k-point mesh. Adsorption energies were found to be converged within <1 meV for E_{cut}^{χ}=200 eV. Further details for convergence can be found in the SI table S6.

Diffusion Barriers

For the calculation of diffusion barriers, we rely on the computational setup used for adsorption energy calculations (see Fig. 1 (a)). We study two different paths for surface diffusion, namely along the [100] direction from the top to the bridge site, Fig. 1 (b), and along the [110] direction from the top to the hollow position on this surface, Fig. 1 (c). For each path, 15 equally spaced points along the high symmetry pathway from the top to the bridge or hollow site were optimized using the following methods keeping the x and y coordinate of the C atom in CO fixed. For PBE, PBE+D2, PBE+D3, BEEF-vdw and RPBE functionals, optimizations were performed using a 10×10×1 k-point mesh. For SCAN, HSE06, and RPA calculations, PBE optimized structures were used. We checked the influence of using PBE structures by comparing the energetics using BEEF-vdW for BEEF-vdW and PBE optimized structures. The values are reported in the SI table S7. Reported DFT energy profiles correspond to single point calculations based on optimized structures at the respective level

of theory with a 8×8×1 k-point mesh for HSE06 and a 15×15×1 k-point mesh for other functionals.

As shown in Fig. 1 (d), the following geometry parameters are analyzed for the structures along the pathways: r_{CO}, the distance between the C and O atom, $d_{CCu,\ z}$, the z coordinate difference between the C atom and the Cu(001) surface plane, $d_{CCu,\ x}/d_{CCu,\ xy}$, the distance between the C and Cu atom projected along the [100]/[110] direction, and θ_{OCz}, the angle spanned by the axis of the CO molecule and the $[00\overline{1}]$ direction. It is worth mentioning that the $d_{CCu,\ x}/d_{CCu,\ xy}$ distances are calculated with respected to the fixed Cu atoms in the third layer of the slab, since this approach mitigates the influence of structural relaxation of the top two layers. Additionally, a potential energy surface for moving CO in the z direction perpendicular to the surface was calculated at the RPA level, where all PBE coordinates were kept fixed, except the z coordinate of C and O, which were shifted away from the surface simultaneously by 0.02 Å, 0.04 Å, and 0.06 Å in z-direction. Detailed energetics are provided in the SI Table S8.

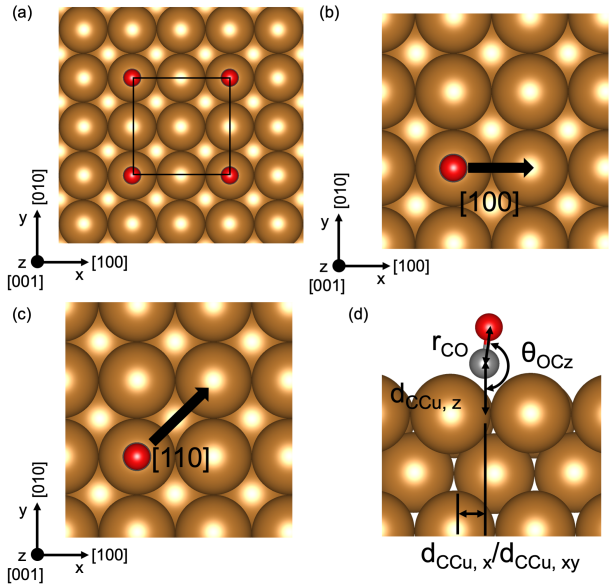

Figure 1: (a) The unit cell of the Cu(001) surface used in this work. (b) The top-bridge-top diffusion pathway along the [100] direction of the Cu(001) surface. (c) The top-hollow-top diffusion pathway along the [110] direction of the Cu(001) surface. (d) The metal carbonyl complex motif showing geometry parameters: r_{CO}, the distance between the C and O atom, $d_{CCu,\ z}$, the z coordinate difference between the C atom and the Cu(001) surface plane, $d_{CCu,\ x}/d_{CCu,\ xy}$, the distance between the C and Cu atom projected along the [100]/[110] direction, and θ_{OCz}, the angle spanned by the axis of the CO molecule and the $[00\bar{1}]$ direction. Cu atoms are shown as brown, O atoms red and C atoms grey.

In all our calculations periodic boundary conditions are used, which leads to all CO molecules diffusing simultaneously, results being given for one CO molecule. To better understand the impact of concerted diffusion and coverage effects, we performed calculations for 4-layer slabs using 3×3 and 4×4 unit cells, which used 7×7×1 and 5×5×1 k-point meshes, respectively.

Computational Setup

All calculations in this paper were performed using the Vienna Ab-Initio Simulation Package[65] (VASP), a code using plane wave basis sets, projector augmented wave[66] (PAW) pseudopotentials, and periodic boundary conditions. In this work we rely on VASP implementations of PBE, PBE+D2, PBE+D3, RPBE, BEEF-vdW, HSE06, and RPA.

GW pseudopotentials were used for all calculations, and more details can be found in the SI Table S11. First order Methfessel-Paxton smearing with sigma value of 0.2 eV was used for all DFT slab optimizations and DFT single point energies whereas gaussian smearing with sigma value of 0.05 eV was used for molecular references. For RPA calculations, gaussian smearing with sigma value of 0.05 eV was used. K-point grids and cut off energies were described in the preceding section.

RPA calculations rely on single-particle orbitals calculated at LDA, GGA, or hybrid functional level of theory. It has been demonstrated that RPA total energies are rather insensitive to the starting orbitals for molecules[47–49] and solids.[35,50] In this work, we rely on RPA calculations using PBE orbitals and PBE one-electron energies (RPA@PBE), which is consistent with previous RPA calculations for metals[36] and metal-O[37] systems. We have further tested RPA based on RPBE orbitals and RPBE one-electron energies (RPA@RPBE) and we find differences smaller than 1 meV for barriers and high symmetry site energy differences. Detailed energetics are provided in the SI table S12.

Results

Surface Energy and Adsorption Enthalpy

We start the discussion of results by focusing on surface energies and adsorption enthalpies and results are shown in Fig. 2. The adsorption enthalpy measures the adsorption strength while the surface energy gives information about the surface stability. The correct description of surface stability is essential as it overall affects the adsorption strength across different adsorbates, and ensures the correct description when impurities, defects, and reconstructions are introduced. In the past it has been shown that multiple density functional theory-based methods exist that describe either the surface energy or the CO adsorption strength accurately but have problems in describing both properties well at the same time.

We find that RPBE, HSE06, and BEEF-vdW, which describe the adsorption enthalpy

accurately, give significantly lower surface energies compared to experimental value. SCAN, which leads to an accurate surface energy, significantly overestimates the adsorption strength. Only RPA leads to surface energies and adsorption enthalpies in close agreement with experimental data. These results agree well with reports in the literature for close packed 111 surfaces, where it was found that for DFT functionals the sum of adsorption enthalpy and surface energy underestimates the experimentally observed values and only RPA leads to reasonable agreement between theory and experiment.[37]

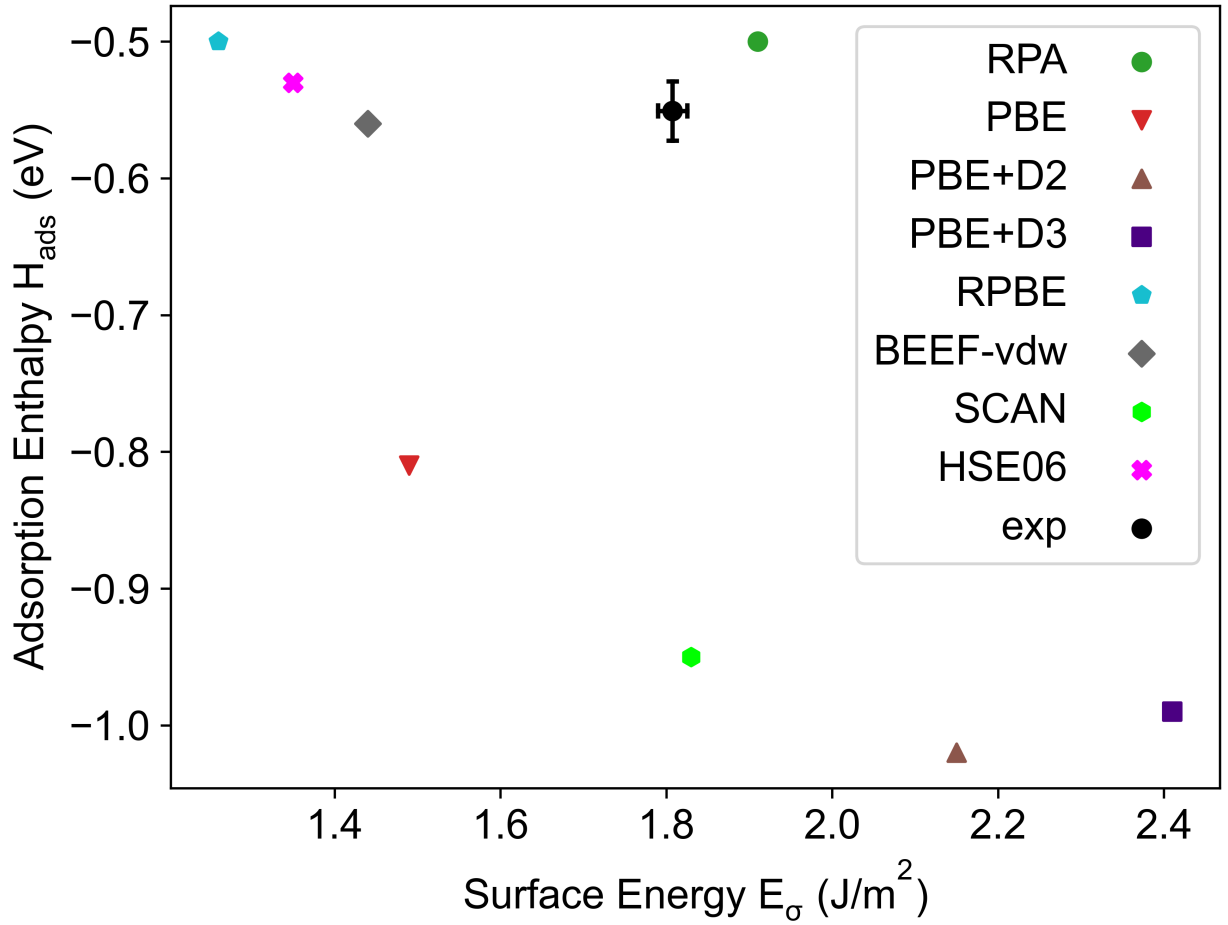

Figure 2: Cu(001) surface energy and CO adsorption enthalpy values of the methods used here. Experimental values are shown with error bar. Experimental surface energy is deduced from liquid-metal data as an average for all surfaces. Surface energy values are shown in the unit of J/m^2 and CO adsorption enthalpy values are shown in unit of eV per CO molecule.

Top-Bridge-Top Diffusion

Subsequently, we study CO diffusion along the [100] direction of the Cu(001) surface, as shown in Fig. 1 (b). In this pathway, the CO molecule is moved from the top to the bridge position along the $d_{CCu,\ x}$ direction and the corresponding energy profile is shown in Fig. 3. In agreement with results for the Cu(111) surface,[37] we find that RPA predicts a preference for CO adsorption in the top position over the bridge position by 114 meV, hence providing the correct site in comparison with experiments. Additionally, the top site preference in RPA slightly increases for a higher k-point sampling (90 meV for 3×3×1 k-point mesh, 113 meV for 8×8×1 k-point mesh). PBE prefers adsorption in the bridge position over the top position by 38 meV. D2 and D3 van der Waals corrections further stabilize the bridge site to a total energy difference of 64 and 42 meV, respectively. SCAN agrees with PBE based functionals on the site preference and predicts the bridge site to be more stable by 21 meV compared to the top site. The RPBE and BEEF-vdW functionals on the other hand give the correct site preference, with bridge-top differences calculated to be 11 and 26 meV. HSE06 leads to results most similar to RPA with a preference for the top site over the bridge site by 108 meV.

In agreement with the significant differences in relative energies between top and bridge positions, diffusion barriers are also vastly different. While the overall barrier for top-bridge diffusion at RPA level is 132 meV (117 meV for 3×3×1 k-point mesh and 130 meV for 8×8×1 k-point mesh, respectively), the lowest barrier for the displacement from top to bridge site is found using PBE-D3 (11 meV). The other values lie between these two extremes with HSE06 leading to a barrier most closely resembling RPA values. BEEF-vdW, even it correctly describes the preferred top site and it adsorption enthalpy, gives a much smaller diffusion barrier (51 meV) linked with a smaller energy difference between top and bridge site. Functionals that prefer the bridge site over the top site (SCAN, PBE and PBE with dispersion correction) lead to the lowest barriers. However, in this case the overall diffusion barrier is obtained when moving from bridge to top site, and not from top to bridge, which

increases these barriers to 60 meV (PBE), 53 meV (PBE-D2), 84 meV (PBE-D3), and 49 meV (SCAN).

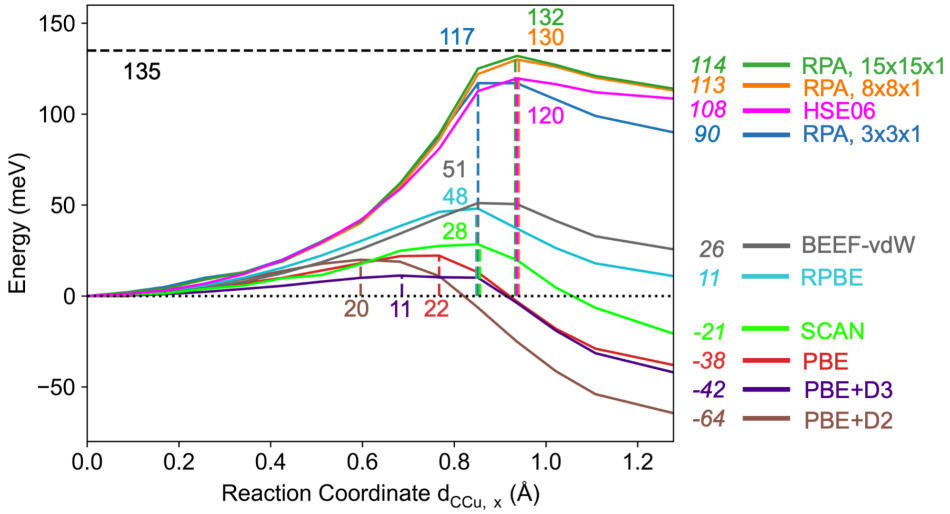

Figure 3: Energy profiles for the CO diffusion from the top site to the bridge site along the [100] direction calculated using different functionals and RPA with different k-point meshes. The distance between the C and Cu atom projected along the [100] direction, $d_{CCu,\ x}$, is utilized as the reaction coordinate. The horizontal dashed black line indicates the experimental barrier,[26] 135 meV. Vertical dashed lines indicate the position of transition states calculated with different methods. Non-italicized values correspond to the barriers and italicized values correspond to the bridge-top energy differences.

Further analysis of the potential energy surface for diffusion shown in Fig. 3 reveals that also the position of the transition state is shifted between different methods. To keep the discussion tractable, we report and discuss structural parameters for PBE, BEEF-vdW, and RPA in the main text. Structural parameters for the other methods are provided in the Supporting Information Table S13. While the PBE and BEEF-vdW transition states lie at $d_{CCu,\ x}$=0.77 Å and 0.85 Å, the RPA transition state lies at $d_{CCu,\ x}$=0.94 Å and therefore later along the reaction coordinate. Given the significant difference in final state energies, a shift in transition state coordinate between the different methods is not unexpected.

We furthermore analyzed the geometries of CO adsorbed in the different positions along the diffusion path and the atomistic structures are shown in Fig. 4. In the top adsorption

site CO adsorbs perpendicular to the surface plane with a r_{CO} (the distance between C and O atoms, see Fig. 1 (d)) value of 1.15 Å for both PBE and BEEF-vdW. (RPA shares the same r_{CO} with PBE since the RPA geometry is only optimized by simultaneously shifting the z coordinate of C and O atoms). This distance slightly increases to 1.17 and 1.16 Å in the bridge position for PBE and BEEF-vdW, respectively. Using PBE we find a $d_{CCu,\ z}$ (the difference in z coordinate between the C atom and the closest Cu surface atom, see Fig. 1 (d)) value of 1.84 Å for the top position and 1.52 Å in the bridge position. Optimizing $d_{CCu,\ z}$ at RPA level leads to an increase of 0.02 Å (top position) and 0.04 Å (bridge position). For the transition state (TS) geometry, it is not surprising to see that RPA gives a TS geometry closer to the bridge site one, since the TS lies later along the pathway, indicated the values for $d_{CCu,\ z}$ of 1.71 Å, 1.70 Å, and 1.60 Åfor PBE, BEEF-vdW, and RPA, respectively.

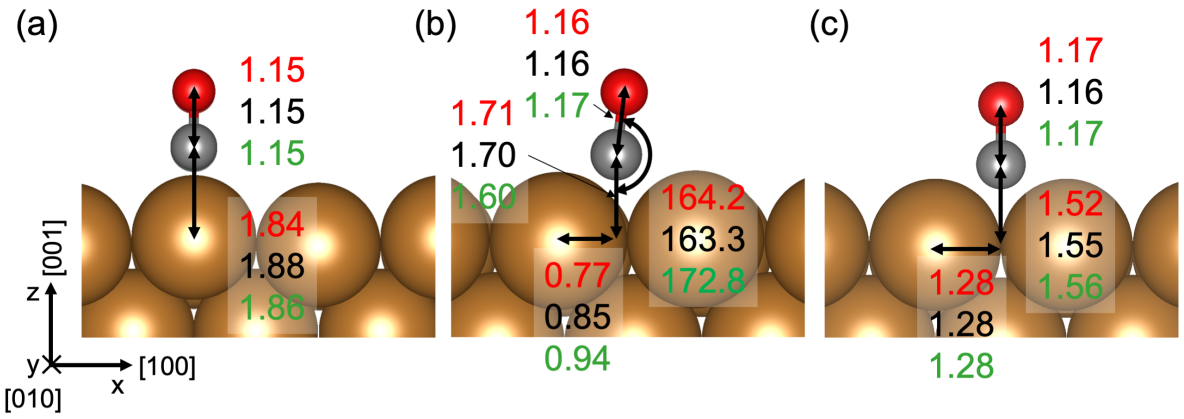

Figure 4: Structures along the [100] diffusion pathway. (a) Top site structure. (b) Transition state structure. (c) Bridge site structure. As defined in Fig. 1 (d), values are shown for r_{CO}, the distance between the C and O atom, $d_{CCu,\ z}$, the z coordinate difference between the C atom and the Cu(001) surface plane, $d_{CCu,\ x}$, the distance between the C and bulk (fixed) Cu atom projected along the [100] direction, and θ_{OCz}, the angle spanned by the axis of the CO molecule and the [00$\bar{1}$] direction. Similar to the color scheme used in the energy profile, values shown in red, black, and green correspond to PBE, BEEF-vdW and RPA results. Presented numbers are given in Å for distances and degree for angles. Cu atoms are shown as brown, O atoms red and C atoms grey. Numerical values for transition state geometries of the other functionals are given in the SI Table S13.

Top-Hollow-Top Diffusion

As a next step we focus on diffusion from the top site to the hollow site along the [110] direction of the Cu(001) surface, as shown in Fig. 1 (c), and the potential energy surface for this process is shown in Fig. 5. Again, a similar picture to top-bridge diffusion emerges, where the top site is the minimum for RPA (245 meV, 234 meV, and 227 meV more stable than the hollow site for 15×15×1, 8×8×1, and 3×3×1 k-point meshes, respectively), while the hollow site is 8 meV more stable using PBE. Similar trends are found for PBD+D2 where the hollow site is stabilized by 31 meV compared to the top site. PBE+D3 and SCAN give the right site preference but with a rather small difference: the top site is 13 meV more stable than hollow site. RPBE and BEEF-vdW functionals give the right site preference with a larger difference: the top site is 89 and 123 meV more stable than the hollow site, respectively. HSE06 functional once again gives results similar to RPA with a top site preference by 254 meV.

Following this trend, diffusion barriers from the top to the hollow position are increased to 250 meV, 241 meV, and 232 meV for RPA with 15×15×1, 8×8×1, and 3×3×1 k-point meshes and to 55 meV for PBE. However, the effective barrier for PBE, which corresponds to diffusion from the hollow to the top site, is only slightly increased to 63 meV compared to the barrier of 60 meV for the bridge-top diffusion. Applying D2 and D3 van der Waals corrections gives slightly lower barriers: 44 and 49 meV, respectively for diffusion from the top site to the hollow site. SCAN, RPBE, and BEEF-vdW functionals predict higher barriers of 75, 106 and 132 meV, respectively. We do not find a local minimum in the hollow site using the HSE06 functional and the overall barrier of 254 meV is again close to the RPA value 250 meV.

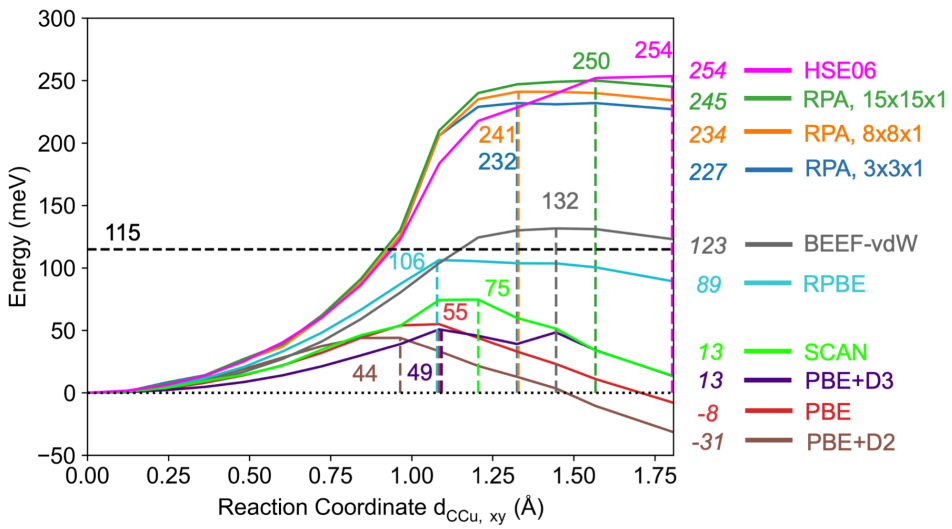

Figure 5: Energy profiles for the CO diffusion from the top site to the hollow site along the [110] direction using different functionals and RPA with different k-point meshes. The distance between the C and Cu atom projected along the [110] direction, $d_{CCu,\ xy}$, is utilized as the reaction coordinate. The horizontal dashed black line indicates the experimental barrier,[26] 115 meV. Vertical dashed lines indicate the position of transition states calculated with different methods. Non-italicized values correspond to the barriers and italicized values correspond to the hollow-top energy differences. Numerical values for transition state geometries of the other functionals are given in the SI Table S13.

Similar to top-bridge diffusion, the RPA transition state lies later along the top-hollow path than the PBE and BEEF-vdW transition state with $d_{CCu,\ xy}$ (the distance along the [110] direction from top to hollow site, see Fig. 1(d)) values of 1.08 Å for PBE, 1.44 for BEEF-vdW, and 1.57 Å (1.32 Å) for RPA with 15×15×1 k-point mesh (8×8×1 and 3×3×1 k-point meshes). The difference in transition state position, also significantly affects the transition state geometry, as shown in Fig. 5 and Fig. 6 (b). r_{CO} increases from 1.17 (PBE) and 1.18 Å (BEEF-vdW) to 1.19 Å (RPA), $d_{CCu,\ z}$ decreases from 1.44 and 1.30 Å to 1.20 Å, and θ_{OCz} increases from 163 and 170 ° to 174°. For adsorption in the hollow position, CO binds perpendicular to the Cu surface, and the geometry parameters are shown in Fig. 6 (c).

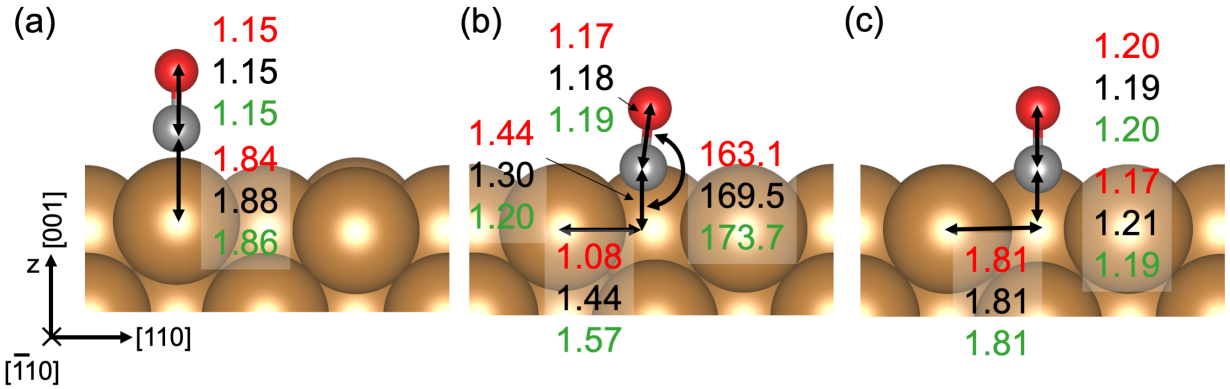

Figure 6: Structures along the [110] diffusion pathway. (a) Top site structure. (b) Transition state structure. (c) Hollow site structure. As defined in Fig. 1 (d), values are shown for r_{CO}, the distance between the C and O atom, $d_{CCu,\ z}$, the z coordinate difference between the C atom and the Cu(001) surface plane, $d_{CCu,\ xy}$, the distance between the C and bulk (fixed) Cu atom projected along the [110] direction, and θ_{OCz}, the angle spanned by the axis of the CO molecule and the [00$\bar{1}$] direction. Similar to the color scheme used in the energy profile, values shown in red, black, and green correspond to PBE, BEEF-vdW and RPA results. Presented numbers are given in Å for distances and degree for angles. Cu atoms are shown as brown, O atoms red and C atoms grey.

Discussion

The results presented in this work agree with data in the literature that RPA is able to predict both, adsorption enthalpies and surface energies correctly, which is not achieved by the other functionals studied in this work. Additionally, RPA and HSE06 correctly predict the preference of CO adsorption in the top position of the Cu(001) surface, which is shared with the BEEF-vdW and RPBE functionals, even though the latter two methods show a smaller preference compared to the former methods. PBE based functionals and the SCAN functional, on the other hand predict the stabilization of CO in the bridge and hollow sites. Qualitatively, these results agree with the work of Schimka et al.,[37] who showed that RPA correctly predicts CO adsorption on the top site on Cu(111), while for the (111) surface PBE shows a preference for CO adsorption in the hollow site. In the following, we restrict the discussion of the diffusion barriers on PBE, BEEF-vdW and RPA, since they provide

qualitatively different descriptions.

The impact of the difference in site preference on the diffusion behavior is significant and becomes apparent when studying the full energy profiles for diffusion along [100] and [110] directions from top to top position, as displayed in Figure 7. At the PBE level, the CO molecule is most of the time at the bridge site and we consider three diffusion pathways: (1) The bridge-top-bridge diffusion pathway in the [100] direction with a barrier of 60 meV. The top site is a local minimum with a barrier of 22 meV to leave it. (2) A bridge-hollow-bridge diffusion pathway in the [100] direction of the surface. (3) A direct bridge-bridge diffusion pathway generally along the [110] direction. We performed climbing image nudged elastic band (CI-NEB)[67] calculations to determine the barrier of pathways (2) and (3). A barrier of 50 meV is found for the bridge-hollow-bridge diffusion pathway and the energy profile is shown in the SI Figure S1. No bridge-bridge diffusion along the [110] direction is found. Considering the barrier values at PBE level, bridge-hollow-bridge diffusion is favored.

At the RPA level, the CO molecule is most of the time at the top site, which agrees with experimental observations.[68] Diffusion along the [100] direction corresponds to a top-bridge-top path with a barrier of 125 meV and the bridge site is metastable, with a barrier of 18 meV to leave it. Diffusion in the [110] direction corresponds to a top-hollow-top path with a barrier of 250 meV, with a very shallow minimum at the hollow site: 5 meV is required to leave it. For both directions, the residence time in the intermediate position is very short, and the diffusion is effectively a single jump from top to top. Considering the barrier values at RPA level, two successive top-bridge-top diffusion processes will be more favored than one top-hollow-top diffusion process, which indicates that the diffusion in the [110] direction may correspond to two combined diffusion processes in perpendicular [100] and [010] directions.

Using the BEEF-vdW functional, the qualitative behavior is similar to the results at RPA level but the barrier values are significantly lower. Diffusion along the [100] direction corresponds to a top-bridge-top path with a barrier of 51 meV and the bridge site is metastable, with a barrier of 25 meV to leave it. Diffusion in the [110] direction corresponds

to a top-hollow-top path with a barrier of 132 meV, with a very shallow minimum at the hollow site, where only 9 meV are required to leave it. However, at BEEF-vdW level, the THT barrier is still higher than the TBT barrier.

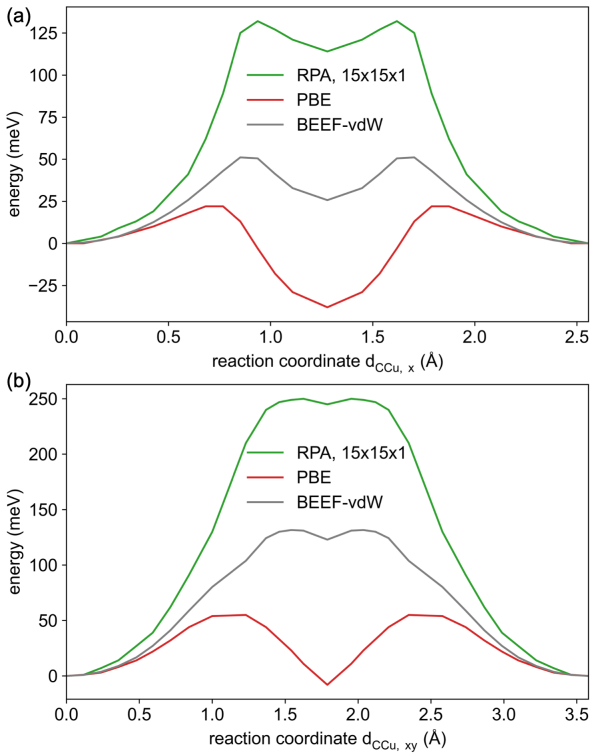

Figure 7: Full energy profile for PBE, BEEF-vdW and RPA for diffusion from top to top site along the [100] (a) and [110] (b) direction. PBE profile is shown as red, BEEF-vdW is shown as grey and RPA is shown as green.

Comparing our results to work in the literature is not entirely straightforward. Initial DFT calculations by Ge and King[27] show a very similar energy profile to our PBE calculations, while Fouquet et al.[28] found a significantly different behavior using localized basis sets, with a maximum at the bridge position, but a significantly lower diffusion barrier compared to this study. Marquardt et al.[29] used potential energy surface achieved by fitting DFT energies and observed a significantly narrower barrier compared to other works and to this study, which lead them to the assumption that tunneling is a significant contributor to the diffusion processes. The shape of the barriers calculated using RPA in this work exclude significant contributions of tunneling to diffusion. The CO molecule would have to tunnel

almost the entire distance between top sites along either direction, which is highly unlikely, due to the high mass of the molecule.

Experimental results for the diffusion barriers for CO on the Cu(001) surface are quite ambiguous. Initial measurements performed by Graham and Toennies[25] suggest a total diffusion barrier of 31±10 meV. However, more refined measurements in combination with molecular dynamic modeling by Alexandrowicz et al.[26] suggest two diffusion pathways with barriers of 135±20 meV along the [100] direction and 115±20 meV along the [110] direction. For the diffusion along the [100] direction RPA leads to quantitative agreement with experiment. At the same time, barriers for diffusion along the [110] direction calculated at BEEF-vdW level of theory show excellent agreement with experimental data. However, both methods agree on a roughly 1:2 ratio in diffusion barriers between the [100] and [110] directions. This disagrees with the observations of Alexandrowicz et al.,[26] which indicate a roughly 1:1 ratio between those two barriers.

To investigate this correlation more closely and understand whether a theoretical method exists that can reproduce a 1:1 ratio in barrier heights, we study the following three relationships, namely (i) energy differences between top/bridge and top/hollow sites, (ii) diffusion barrier in [100] direction and top/bridge energy difference, and (iii) diffusion barrier in [110] direction and top/hollow energy difference. We find that all three parameter groups follow linear relationships with R^2 values larger than 0.96 (see SI Fig. S2). Using these relationships, it is now possible to plot forward and backwards barriers for diffusion in [100] and [110] direction with respect to the top/bridge energy difference. We find that no point exists, where a 1:1 ratio in activation energies in both diffusion directions can be found, when CO preferentially adsorbs in the top position (see SI Fig. S3). Additionally, it is important to notice that the TBT barriers are always lower than the THT barriers, which disagrees with experimental findings.

The reasons for the discrepancy between experimental data and results from our study are not entirely clear. One potential reason for the mismatch is a difference in coverage. While

our computational work focuses on a 2×2 unit cell with a coverage of θ=1/4 monolayers (ML), experimental results were measured for a coverage of θ=0.1 ML. Matching the experimental coverage would require modeling a 3×3 unit cell, which is beyond our current computational capability at RPA level. To estimate the impact of coverage effects, we extrapolated them based on the impact of PBE calculations by using

$$E^{RPA}(\theta = \frac{1}{x}ML) = E^{RPA}(\theta = \frac{1}{4}ML) + E^{PBE}(\theta = \frac{1}{x}ML) - E^{PBE}(\theta = \frac{1}{4}ML) \quad (6)$$

The low coverage calculations are performed on 3×3 surface, $\theta = \frac{1}{9}$, and 4×4 surface, $\theta = \frac{1}{16}$. The results are shown in the SI Fig. S2. For the diffusion along the [100] direction, no significant changes are observed: the energetic differences are always smaller than 10 meV. For the diffusion along the [110] direction, coverage effects slightly decrease the barrier from 250 meV at $\theta = \frac{1}{4}$ to 232 meV at $\theta = \frac{1}{9}$ and 219 meV at $\theta = \frac{1}{16}$. Even though this change in energetics when extrapolating results to lower coverages is not sufficient to reach agreement between our calculations and experiments, coverage effects seem to lower barriers along the top-hollow-top pathway more than along the top-bridge top pathway. Additionally, the significant change of the TS position ($d_{CCu,\ xy}$ values from 1.62 Å to 1.37 Å) and the overall profile shape for diffusion along the [110] direction indicate that non-trivial coverage effects might exist. It is possible that these coverage effects cannot be fully captured at PBE level. In future work it will be interesting to see how the coverage effects are present at RPA level, which are not accessible for us at the moment due to the excessive computational cost. That being said, diffusion barriers still follow the linear trends discussed in the SI section S12, which indicates that coverage effects cannot recover the behavior described by Alexandrowicz et al..[26]

Results presented in this work reveal a significant mismatch between all theoretical methods and experimental data. At this moment in time the source of this mismatch is not entirely clear. One possibility is that a non-trivial diffusion pathway in either direction has

been missed in our study. Another possibility is that experimental measurements will need to be revisited and reinterpreted based on the findings in this work.

Conclusion

In this work we describe our efforts to model the diffusion of CO on the Cu(001) surface using RPA and compare the results with calculations using different GGA, metaGGA, and hybrid functionals. In a first step we present a k-space embedding strategy for RPA calculations, which significantly reduces the computational cost. We consider the adsorption enthalpies and surface energies using the aforementioned methods. Subsequently we apply this methodology to CO diffusion along two high-symmetry directions of the surface, namely (i) top-bridge-top diffusion along the [100] direction and (ii) top-hollow-top diffusion along the [110] direction. We find that RPA appears to be the only method giving the correct site preference and adsorption enthalpy for CO, and surface energy for Cu(001). DFT methods that give correct site preference (RPBE, BEEF-vdW, and HSE06) may suffer from underestimated surface energies. Our results furthermore reveal qualitative differences in the description of diffusion barriers compared to experiments. While RPA and BEEF-vdW are able to quantatively correctly predict one of the diffusion barriers, no functional reproduces the experimentally observed ratio for diffusion barriers. Since this is a phenomenon shared by all methods, we conclude that it might be necessary to revisit the interpretation of the experimental data.

The results presented in this work show that the incorrectly predicted adsorption site preference for CO on transition metal surfaces using different functionals can qualitatively and quantitatively alter predictions for diffusion pathways of CO on transition metal surfaces. It is well conceivable that similar differences exist for other reactions that involve CO on transition metal surfaces. The shortcomings of the functionals considered, especially the underestimated surface energies indicate that it is necessary to move to more accurate

methods, such as RPA, when modeling adsorption across different species. We expect that the methods and results presented here will encourage further investigations on fundamental interactions between CO related species on transition metal surfaces, which are necessary to understand thermocatalytic and electrocatalytic reactions involving CO related species on Cu and other transition metal surfaces.

Acknowledgement

The calculations were performed on the Hoffman2 cluster at UCLA Institute for Digital Research and Education (IDRE) and the Extreme Science and Engineering Discovery Environment (XSEDE),[69] which is supported by National Science Foundation grant number ACI-1548562, through allocation TG-CHE170060. F. Göltl acknowledges support from the College of Agriculture and Life Science at the University of Arizona.

Associated Content

Supplementary Information: Convergence of RPA diffusion energetics with respect to E_{cut}^{χ} (Table S1); Numerical validation of k-space ONIOM like scheme (Table S2, Fig. S1); Lattice parameters and surface energies calculated (Table S3); Vacuum separation influence on energetics (Table S4); Details of the adsorption enthalpy calculations (Table S5); Convergence of RPA CO adsorption energy with respect to E_{cut}^{χ} (Table S6); BEEF-vdW energy profile with PBE geometry (Table S7); Energetics of z shifted structures at RPA Level (Table S8, S9, and S10); Pseudopotential details (Table S11); Influence of RPA starting orbitals (Table S12); Geometry parameters of all the functionals (Table S13); Linear relationships of energy differences and barriers (Fig. S2 and S3); Bridge-hollow-bridge diffusion at PBE level (Fig. S4); Energy profiles with coverage effects (Fig. S5).

References

(1) Medford, A. J.; Lausche, A. C.; Abild-Pedersen, F.; Temel, B.; Schjødt, N. C.; Nørskov, J. K.; Studt, F. Activity and Selectivity Trends in Synthesis Gas Conversion to Higher Alcohols. *Top. Catal.* **2013**, *57*, 135–142.

(2) Schumann, J.; Medford, A. J.; Yoo, J. S.; Zhao, Z.-J.; Bothra, P.; Cao, A.; Studt, F.; Abild-Pedersen, F.; Nørskov, J. K. Selectivity of Synthesis Gas Conversion to C2+ Oxygenates on fcc(111) Transition-Metal Surfaces. *ACS Catal.* **2018**, *8*, 3447–3453.

(3) Kattel, S.; Ramírez, P. J.; Chen, J. G.; Rodriguez, J. A.; Liu, P. Active sites for CO2 hydrogenation to methanol on Cu/ZnO catalysts. *Science* **2017**, *355*, 1296–1299.

(4) Behrens, M.; Studt, F.; Kasatkin, I.; Kuhl, S.; Havecker, M.; Abild-Pedersen, F.; Zander, S.; Girgsdies, F.; Kurr, P.; Kniep, B.-L.; Tovar, M.; Fischer, R.; Norskov, J.; Schlogl, R. The Active Site of Methanol Synthesis over Cu/ZnO/Al2O3 Industrial Catalysts. *Science* **2012**, *336*, 893–897.

(5) Campbell, C. T.; Daube, K. A surface science investigation of the water-gas shift reaction on Cu (111). *J. Catal.* **1987**, *104*, 109–119.

(6) Gokhale, A. A.; Dumesic, J. A.; Mavrikakis, M. On the Mechanism of Low-Temperature Water Gas Shift Reaction on Copper. *J. Am. Chem. Soc.* **2008**, *130*, 1402–1414.

(7) Nitopi, S.; Bertheussen, E.; Scott, S. B.; Liu, X.; Engstfeld, A. K.; Horch, S.; Seger, B.; Stephens, I. E.; Chan, K.; Hahn, C.; Nørskov, J. K.; Jaramillo, T. F.; Chorkendorff, I. Progress and Perspectives of Electrochemical CO2 Reduction on Copper in Aqueous Electrolyte. *Chem. Rev.* **2019**, *119*, 7610–7672.

(8) Nørskov, J.; Bligaard, T.; Rossmeisl, J.; Christensen, C. Towards the computational design of solid catalysts. *Nat. Chem.* **2009**, *1*, 37–46.

(9) Bruix, A.; Margraf, J. T.; Andersen, M.; Reuter, K. First-principles-based multiscale modelling of heterogeneous catalysis. *Nat. Catal.* **2019**, *2*, 659–670.

(10) Sutton, J. E.; Vlachos, D. G. Building large microkinetic models with first-principles' accuracy at reduced computational cost. *Chem. Eng. Sci.* **2015**, *121*, 190–199.

(11) Reuter, K. Ab Initio Thermodynamics and First-Principles Microkinetics for Surface Catalysis. *Catal. Lett.* **2016**, *146*, 541–563.

(12) Andersen, M.; Panosetti, C.; Reuter, K. A Practical Guide to Surface Kinetic Monte Carlo Simulations. *Front. Chem.* **2019**, *7*, 202.

(13) Hohenberg, P.; Kohn, W. Inhomogeneous Electron Gas. *Phys. Rev.* **1964**, *136*, B864–B871.

(14) Kohn, W.; Sham, L. Self-Consistent Equations Including Exchange and Correlation Effects. *Phys. Rev.* **1965**, *140*, A1133–A1138.

(15) Perdew, J. P.; Chevary, J.; Vosko, S.; Jackson, K. A.; Pederson, M. R.; Singh, D.; Fiolhais, C. Atoms, molecules, solids, and surfaces: Applications of the generalized gradient approximation for exchange and correlation. *Phys. Rev. B* **1992**, *46*, 6671–6687.

(16) Gil, A. Site preference of CO chemisorbed on Pt(111) from density functional calculations. *Surf. Sci.* **2003**, *530*, 71–87.

(17) Gajdoš, M.; Eichler, A.; Hafner, J. CO adsorption on close-packed transition and noble metal surfaces: Trends from ab initio calculations. *J. Phys. Condens. Matter* **2004**, *16*, 1141.

(18) Feibelman, P. J.; Hammer, B.; Nørskov, J.; Wagner, F.; Scheffler, M.; Stumpf, R.; Watwe, R.; Dumesic, J. The CO/Pt(111) Puzzle. *J. Phys. Chem. B* **2000**, *105*, 4018–4025.

(19) Kresse, G.; Gil, A.; Sautet, P. Significance of single-electron energies for the description of CO on Pt(111). *Phys. Rev. B* **2003**, *68*, 073401.

(20) Cheng, T.; Xiao, H.; Goddard, W. A. Free-Energy Barriers and Reaction Mechanisms for the Electrochemical Reduction of CO on the Cu(100) Surface, Including Multiple Layers of Explicit Solvent at pH 0. *J. Phys. Chem. Lett.* **2015**, *6*, 4767–4773.

(21) Peterson, A. A.; Abild-Pedersen, F.; Studt, F.; Rossmeisl, J.; Nørskov, J. K. How copper catalyzes the electroreduction of carbon dioxide into hydrocarbon fuels. *Energy Environ. Sci.* **2010**, *3*, 1311.

(22) Kortlever, R.; Shen, J.; Schouten, K. J. P.; Calle-Vallejo, F.; Koper, M. T. Catalysts and Reaction Pathways for the Electrochemical Reduction of Carbon Dioxide. *J. Phys. Chem. Lett.* **2015**, *6*, 4073–4082.

(23) Lum, Y.; Cheng, T.; Goddard, W. A.; Ager, J. W. Electrochemical CO Reduction Builds Solvent Water into Oxygenate Products. *J. Am. Chem. Soc.* **2018**, *140*, 9337–9340.

(24) Kuhl, K. P.; Cave, E. R.; Abram, D. N.; Jaramillo, T. F. New insights into the electrochemical reduction of carbon dioxide on metallic copper surfaces. *Energy Environ. Sci.* **2012**, *5*, 7050.

(25) Graham, A. P.; Hofmann, F.; Toennies, J. P.; Williams, G. P.; Hirschmugl, C. J.; Ellis, J. A high resolution helium atom scattering and far infrared study of the dynamics and the lateral potential energy surface of CO molecules chemisorbed on Cu(001). *J. Chem. Phys.* **1998**, *108*, 7825–7834.

(26) Alexandrowicz, G.; Jardine, A.; Fouquet, P.; Dworski, S.; Allison, W.; Ellis, J. Observation of Microscopic CO Dynamics on Cu(001) UsingH3eSpin-Echo Spectroscopy. *Phys. Rev. Lett.* **2004**, *93*, 156103.

(27) Ge, Q.; King, D. Response to "Comment on 'Surface diffusion potential energy surfaces from first principles"' [J. Chem. Phys. 114, 1051 (2001)]. *J. Chem. Phys.* **2001**, *114*, 1053.

(28) Fouquet, P.; Olsen, R. A.; Baerends, E. J. Diffusion and vibration of CO molecules adsorbed on a Cu(100) surface: A periodic density functional theory study. *J. Chem. Phys.* **2003**, *119*, 509–514.

(29) Zanuttini, D.; Gatti, F.; Marquardt, R. CO quantum dynamics diffusion on Cu(1 0 0). *Chem. Phys.* **2018**, *509*, 3–12.

(30) Grüneis, A.; Marsman, M.; Harl, J.; Schimka, L.; Kresse, G. Making the random phase approximation to electronic correlation accurate. *J. Chem. Phys.* **2009**, *131*, 154115.

(31) Nozières, P.; Pines, D. Correlation Energy of a Free Electron Gas. *Phys. Rev.* **1958**, *111*, 442–454.

(32) Harl, J.; Kresse, G. Cohesive energy curves for noble gas solids calculated by adiabatic connection fluctuation-dissipation theory. *Phys. Rev. B* **2008**, *77*, 045136.

(33) Gunnarsson, O.; Lundqvist, B. Exchange and correlation in atoms, molecules, and solids by the spin-density-functional formalism. *Phys. Rev. B* **1976**, *13*, 4274–4298.

(34) Langreth, D. C.; Perdew, J. P. Exchange-correlation energy of a metallic surface: Wave-vector analysis. *Phys. Rev. B* **1977**, *15*, 2884–2901.

(35) Harl, J.; Kresse, G. Accurate Bulk Properties from Approximate Many-Body Techniques. *Phys. Rev. Lett.* **2009**, *103*, 056401.

(36) Schimka, L.; Gaudoin, R.; Klimeš, J.; Marsman, M.; Kresse, G. Lattice constants and cohesive energies of alkali, alkaline-earth, and transition metals: Random phase approximation and density functional theory results. *Phys. Rev. B* **2013**, *87*, 214102.

(37) Schimka, L.; Harl, J.; Stroppa, A.; Grüneis, A.; Marsman, M.; Mittendorfer, F.; Kresse, G. Accurate surface and adsorption energies from many-body perturbation theory. *Nat. Mater.* **2010**, *9*, 741–744.

(38) Perdew, J. P.; Burke, K.; Ernzerhof, M. Generalized Gradient Approximation Made Simple. *Phys. Rev. Lett.* **1996**, *77*, 3865–3868.

(39) Grimme, S. Semiempirical GGA-type density functional constructed with a long-range dispersion correction. *J. Comput. Chem.* **2006**, *27*, 1787–1799.

(40) Grimme, S.; Antony, J.; Ehrlich, S.; Krieg, H. A consistent and accurate ab initio parametrization of density functional dispersion correction DFT-D for the 94 elements H-Pu. *J. Chem. Phys.* **2010**, *132*, 154104.

(41) Hammer, B.; Hansen, L.; Nørskov, J. Improved adsorption energetics within density-functional theory using revised Perdew-Burke-Ernzerhof functionals. *Phys. Rev. B* **1999**, *59*, 7413–7421.

(42) Wellendorff, J.; Lundgaard, K. T.; Møgelhøj, A.; Petzold, V.; Landis, D. D.; Nørskov, J. K.; Bligaard, T.; Jacobsen, K. W. Density functionals for surface science: Exchange-correlation model development with Bayesian error estimation. *Phys. Rev. B* **2012**, *85*, 235149.

(43) Sun, J.; Ruzsinszky, A.; Perdew, J. P. Strongly Constrained and Appropriately Normed Semilocal Density Functional. *Phys. Rev. Lett.* **2015**, *115*, 036402.

(44) Krukau, A. V.; Vydrov, O. A.; Izmaylov, A. F.; Scuseria, G. E. Influence of the exchange screening parameter on the performance of screened hybrid functionals. *J. Chem. Phys.* **2006**, *125*, 224106.

(45) Adler, S. L. Quantum Theory of the Dielectric Constant in Real Solids. *Phys. Rev.* **1962**, *126*, 413–420.

(46) Wiser, N. Dielectric Constant with Local Field Effects Included. *Phys. Rev.* **1963**, *129*, 62–69.

(47) Furche, F. Developing the random phase approximation into a practical post-Kohn–Sham correlation model. *J. Chem. Phys.* **2008**, *129*, 114105.

(48) Fuchs, M.; Gonze, X. Accurate density functionals: Approaches using the adiabatic-connection fluctuation-dissipation theorem. *Phys. Rev. B* **2002**, *65*, 235109.

(49) Ren, X.; Rinke, P.; Scheffler, M. Exploring the random phase approximation: Application to CO adsorbed on Cu(111). *Phys. Rev. B* **2009**, *80*, 045402.

(50) Zhang, G.-X.; Tkatchenko, A.; Paier, J.; Appel, H.; Scheffler, M. van der Waals Interactions in Ionic and Semiconductor Solids. *Phys. Rev. Lett.* **2011**, *107*, 245501.

(51) Vreven, T.; Byun, K. S.; Komáromi, I.; Dapprich, S.; Montgomery, J. A.; Morokuma, K.; Frisch, M. J. Combining Quantum Mechanics Methods with Molecular Mechanics Methods in ONIOM. *J. Chem. Theory Comput.* **2006**, *2*, 815–826.

(52) Chung, L. W.; Sameera, W.; Ramozzi, R.; Page, A. J.; Hatanaka, M.; Petrova, G. P.; Harris, T. V.; Li, X.; Ke, Z.; Liu, F.; Li, H.-B.; Ding, L.; Morokuma, K. The ONIOM Method and Its Applications. *Chem. Rev.* **2015**, *115*, 5678–5796.

(53) Göltl, F.; Houriez, C.; Guitou, M.; Chambaud, G.; Sautet, P. Importance of a Nonlocal Description of Electron–Electron Interactions in Modeling the Dissociative Adsorption of H2 on Cu(100). *J. Phys. Chem. C* **2014**, *118*, 5374–5382.

(54) Hu, Q.-M.; Reuter, K.; Scheffler, M. Towards an Exact Treatment of Exchange and Correlation in Materials: Application to the "CO Adsorption Puzzle" and Other Systems. *Phys. Rev. Lett.* **2007**, *98*, 176103.

(55) Sauer, J. Ab Initio Calculations for Molecule–Surface Interactions with Chemical Accuracy. *Acc. Chem. Res.* **2019**, *52*, 3502–3510.

(56) Libisch, F.; Huang, C.; Carter, E. A. Embedded Correlated Wavefunction Schemes: Theory and Applications. *Acc. Chem. Res.* **2014**, *47*, 2768–2775.

(57) Zhang, X.; Carter, E. A. Subspace Density Matrix Functional Embedding Theory: Theory, Implementation, and Applications to Molecular Systems. *J. Chem. Theory Comput.* **2018**, *15*, 949–960.

(58) Yu, K.; Carter, E. A. Extending density functional embedding theory for covalently bonded systems. *Proc. Natl. Acad. Sci. U.S.A.* **2017**, *114*, E10861–E10870.

(59) Huang, C.; Pavone, M.; Carter, E. A. Quantum mechanical embedding theory based on a unique embedding potential. *J. Chem. Phys.* **2011**, *134*, 154110.

(60) Libisch, F.; Huang, C.; Liao, P.; Pavone, M.; Carter, E. A. Origin of the Energy Barrier to Chemical Reactions ofO2on Al(111): Evidence for Charge Transfer, Not Spin Selection. *Phys. Rev. Lett.* **2012**, *109*, 198303.

(61) Sharifzadeh, S.; Huang, P.; Carter, E. Embedded Configuration Interaction Description of CO on Cu(111): Resolution of the Site Preference Conundrum. *J. Phys. Chem. C* **2008**, *112*, 4649–4657.

(62) Schimka, L. Application of the random phase approximation to complex problems in materials science. Ph.D. thesis, University of Vienna, retrieved from othes.univie.ac.at, 2012.

(63) Janthon, P.; Luo, S.; Kozlov, S. M.; Vines, F.; Limtrakul, J.; Truhlar, D. G.; Illas, F. Bulk properties of transition metals: A challenge for the design of universal density functionals. *J. Chem. Theory Comput.* **2014**, *10*, 3832–3839.

(64) Lebègue, S.; Harl, J.; Gould, T.; Ángyán, J.; Kresse, G.; Dobson, J. Cohesive Properties and Asymptotics of the Dispersion Interaction in Graphite by the Random Phase Approximation. *Phys. Rev. Lett.* **2010**, *105*, 196401.

(65) Kresse, G.; Hafner, J. Ab initio molecular dynamics for liquid metals. *Phys. Rev. B* **1993**, *47*, 558.

(66) Blöchl, P. Projector augmented-wave method. *Phys. Rev. B* **1994**, *50*, 17953–17979.

(67) Henkelman, G.; Uberuaga, B. P.; Jónsson, H. A climbing image nudged elastic band method for finding saddle points and minimum energy paths. *J. Chem. Phys.* **2000**, *113*, 9901–9904.

(68) Truong, C. M.; Rodriguez, J.; Goodman, D. CO adsorption isotherms on Cu(100) at elevated pressures and temperatures using infrared reflection absorption spectroscopy. *Surf. Sci.* **1992**, *271*, L385–L391.

(69) Towns, J.; Cockerill, T.; Dahan, M.; Foster, I.; Gaither, K.; Grimshaw, A.; Hazlewood, V.; Lathrop, S.; Lifka, D.; Peterson, G. D.; Roskies, R.; Scott, J. R.; Wilkins-Diehr, N. XSEDE: Accelerating Scientific Discovery. *Comput. Sci. Eng.* **2014**, *16*, 62–74.

Graphical TOC Entry